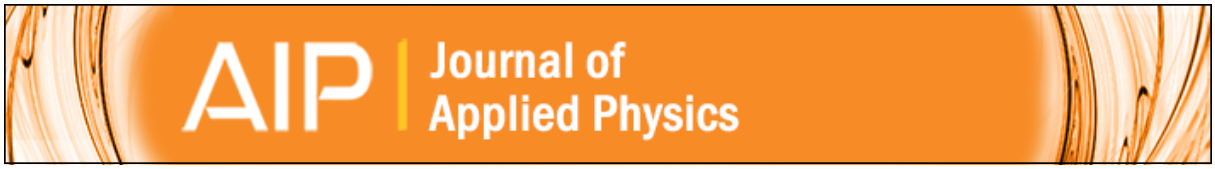

Molecular dynamic simulation of tip-polymer interaction in tapping-mode atomic force microscopy

N. Onofrio, G. N. Venturini, and A. Strachan

Citation: Journal of Applied Physics **114**, 094309 (2013); doi: 10.1063/1.4820256
View online: http://dx.doi.org/10.1063/1.4820256
View Table of Contents: http://scitation.aip.org/content/aip/journal/jap/114/9?ver=pdfcov
Published by the AIP Publishing

Advertisement:

[This article is copyrighted as indicated in the abstract. Reuse of AIP content is subject to the terms at: http://scitation.aip.org/termsconditions. Downloaded to] IP: 131.215.71.79 On: Thu, 17 Oct 2013 14:48:06

Molecular dynamic simulation of tip-polymer interaction in tapping-mode atomic force microscopy

N. Onofrio,[1] G. N. Venturini,[2] and A. Strachan[1,a)]
[1]*School of Materials Engineering, Purdue University, West Lafayette, Indiana 47906, USA*
[2]*Division of Engineering and Applied Science, California Institute of Technology, Pasadena, California 91125, USA*

(Received 8 April 2013; accepted 18 August 2013; published online 6 September 2013)

We present a molecular dynamic study of the interaction between an amorphous silica tip (SiO_2) and an amorphous poly-(methyl-methacrylate) substrate under conditions relevant for tapping-mode atomic force microscopy. To capture the actual dynamics of the tip, we use the dynamic contact simulation method [Kim *et al.*, J. Appl. Phys. **112**, 094325 (2012)]. We obtain force-displacement relationships both for neat polymer substrates and a sample with a sub-surface nanotube and extract the local stiffness and energy dissipation per cycle. The simulations capture non-trivial aspects of the interaction that originate from the viscoelastic nature of the polymer including an increase in repulsive interaction force during approach with tip velocity and an increase in adhesion during retraction with decreasing tip velocity. Scans of local stiffness and dissipation over the samples reveal intrinsic variability in the amorphous polymer but also the effect of local surface topography on the extracted properties as well as the ability of the method to detect a sub-surface nanotube. This insight and quantitative data should be valuable to interpret the results of atomic force microscopy studies. © *2013 AIP Publishing LLC*. [http://dx.doi.org/10.1063/1.4820256]

I. INTRODUCTION

Atomic force microscopy (AFM) is a powerful tool for imaging and nanostructure manipulation with atomic resolution.[1] In contrast with the scanning tunneling microscopy (STM), proposed by Binning *et al.* in the 1980s,[2] AFM allows the investigation of both conductors *and* insulators. During the last two decades, several AFM operating modes have been proposed and investigated.[3] In dynamic mode (also known as tapping-mode), a cantilever with a tip is excited at a frequency near resonance and is brought close to the surface of interest.[4–8] The changes in amplitude and frequency as well as phase shift of the oscillations that originate from tip-sample interaction are then used to extract surface topography of the sample of interest. Dynamic mode AFM has the advantage of not requiring vacuum and the intermittent interaction attenuates surface damage.[5] Therefore, tapping mode AFM has been widely used to study various soft materials ranging from polymers to biomolecules.[6,9,10]

More recently, T-shaped AFM cantilevers have been introduced to improve the resolution and recover information about the tip-sample force interaction.[11] In this method, the tip is offset from the long axis of the cantilever. As a consequence, torsional harmonic of the cantilever and high frequency components of the tip-sample forces can be extracted resulting in time-resolved tapping force curves (cf. force-displacement curves). This new technique allows mapping the local elastic modulus[12] with very high sensitivity for variety of materials.[13]

Despite the growing importance and potential of such techniques in material science, the link between the actual observables (amplitude, resonance frequency, phase shift, or even force-displacement curves) and the underlying material properties (e.g., local viscoelasticity) remains tenuous. As a consequence, it is still challenging to interpret AFM results and complex models are needed to relate observables to quantities of interest. Continuum mechanics can be used to model the dynamics of the cantilever;[14–17] but these simulations require a tip-sample interaction relationship as an input. Such tip-sample interaction depends on both the properties of the tip and sample and can be modeled using molecular dynamic (MD) or quantum mechanic simulations.[18–20] In this paper, we characterize tip-substrate interaction using MD with the dynamic contact simulation (DCS) method.[21] Current computational capabilities admit atomistic simulation with spatial (size of the tip and sample) and temporal (duration of the interaction) scales approaching those of the experiments making quantitative, direct comparisons with experiments possible in the near future. Such direct comparisons would be possible by combining tip-sample relationships from atomistic with continuum simulations of the cantilever dynamics to predict the experimental observables.[22] We envision this type of approach to be critical for the accurate interpretation of AFM experiments.

Previous MD investigations reported important insight on tip-substrate interaction.[22–32] Both constant-force and constant-height dissipation maps have been used to characterize surfaces on model systems.[25,33] More recently, MD simulations of the interaction between a carbon nanotube (CNT)[34] or a fullerene molecule[35] and the tip provided useful information for the analysis of AFM results. This prior work described the dynamics of the tip as it interacts with the sample as in our case we use the DCS model to reproduce as closely as possible the conditions acting in tapping-mode AFM experiments via MD simulations.

a)Electronic mail: strachan@purdue.edu.

 © 2013 AIP Publishing LLC

[This article is copyrighted as indicated in the abstract. Reuse of AIP content is subject to the terms at: http://scitation.aip.org/termsconditions. Downloaded to] IP: 131.215.71.79 On: Thu, 17 Oct 2013 14:48:06

This paper is organized as follows. We introduce the computational details and the DCS model in Sec. II. Section III focuses on the effect of the initial tip-sample distance, interaction velocity, and tip/sample size on the resulting interaction. Section IV shows surface property maps using two modes: the constant height and the topographic modes (TMs). Finally, we discuss the results and draw conclusions in Sec. V.

II. METHODOLOGY

A. Computational details

The simulation cells include a half-sphere of amorphous SiO_2 (the tip)[36] and a poly-(methyl-methacrylate) (PMMA) slab as shown in the snapshot in Figure 1. We use the LAMMPS MD package developed at Sandia National Laboratories[37] and the DREIDING force field to describe the interaction between atoms.[38] A cutoff of 1.2 nm is used for the non-bonded interactions with the particle-particle-particle mesh method for electrostatics.[39] The equations of motion are solved using the rRESPA multi-timescale integrator to speed up the simulations[40] with a timestep of 4 fs. Our prior work on thermoset[41,42] and thermoplastic[43] polymers shows that Dreiding provides an accurate description of thermo-mechanical properties of these materials.

Amorphous PMMA slabs, with periodic boundary conditions along the x and y directions and free surfaces normal to z, of different sizes are used for the simulations; in all cases, the slabs contain 98-monomer-long chains. We use two different sizes of polymer slabs based on the diameter of the tip to minimize boundary conditions effects. A *large* simulation cell contains 160 chains (230 720 atoms in the polymer) and measures 9.6 nm in thickness with 16.5×16.5 nm^2 in cross-section; a *small* simulation cell contains 40 chains (57 680 atoms in the polymer) with a thickness of 16 nm and cross section area of 5.8×5.8 nm^2. In all cases, the slab thickness is enough to limit boundary effect across the free surface in the z direction taking into account that the tip will indent a maximum distance of 1.85 nm in the polymer. A third sample is investigated to explore the effects of a subsurface CNT on tip-substrate interactions. This sample contains 40 PMMA chains and a total 59 040 atoms (including CNT); it measures 11 nm in thickness and 8.2×8.2 nm^2 in cross section. The CNT is located approximately 1.0 nm below the surface.

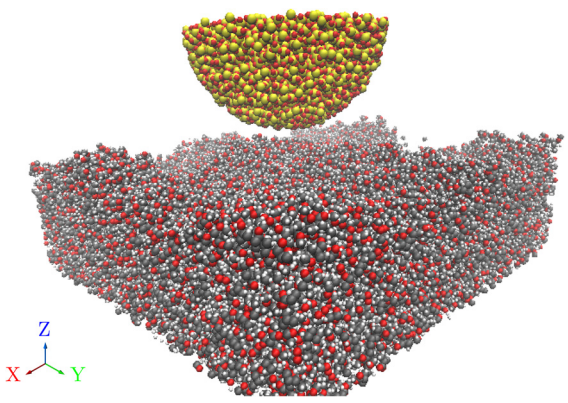

FIG. 1. Molecular structure of the simulation box containing an amorphous silica tip and a PMMA sample (white spheres: H, gray: C, red: O, and yellow: Si).

The slabs are created and equilibrated at $T = 600$ K (over their glass transition temperature) for 2400 ps and then cooled down to 300 K under isothermal and isochoric conditions (NVT ensemble) at a rate of 25 K per 100 ps. The slab is then relaxed at 300 K under isothermal isobaric conditions (NPT ensemble) under atmospheric stress in the directions normal to the free surface during 200 ps. Finally, the samples are equilibrated under isochoric, isothermal conditions (NVT ensemble) at 300 K for an additional 150 ps (setting the simulation cell parameters to the average values computed during the last 100 ps of the NPT equilibration). The composite sample (PMMA and CNT) is obtained from a MD simulation of the process of wrapping a CNT into the polymer. Specifically, we place a CNT on the surface of the PMMA slab and carry out a MD simulation at $T = 600$ K for 400 ps under constant stress and temperature conditions. This time is enough for the surface energetics to result in the CNT moving into the polymer slab. The resulting structure is annealed to $T = 300$ K and relaxed using the same protocol than the neat PMMA slab. Additional details and thermo-mechanical properties of these slabs can be found in Ref. 45.

The tip is modeled by a half sphere of amorphous SiO_2 and we chose to investigate three relevant diameters (4, 8, and 12 nm). The tip moves as a rigid body and rotations and translations in the x-y (normal to the surface) are not allowed to mimic the mechanical constraints of the cantilever. We remove the atoms located in the inner shell of the larger tips (8 and 12 nm of diameter) in order to reduce the number of atoms in the simulation cell. These hollow half spheres have a wall thickness of 2.0 nm, greater than the real space cutoff for non-bond interactions. The small tip (4 nm of diameter) is combined with the small neat PMMA slab (this setup will be labeled as small/4 nm) and the composite sample (cnt/4 nm). The large slab is combined with the medium tip (large/8 nm) and the large tip (large/12 nm). Table I summarizes the samples and additional information, and molecular structures can be found in the supplementary material.[44]

B. Dynamic contact simulations

The SiO_2 tip is treated as a rigid body and interacts with the polymer slab via van der Waals and electrostatics interactions (see supplementary material[44] for details). The dynamical interaction between the tip and polymer is modeled using the DCS method.[21] This approach uses MD simulations with an initial condition consisting of tip and sample

TABLE I. Details on the systems studied in this paper.

Label	Slab ($l \times w \times h$ nm^3)	Atoms in the polymer	Tip diameter (nm)	Atoms in the tip
Small/4nm	$5.8 \times 5.8 \times 16$	57 680	4	1107
Large/8 nm	$16.5 \times 16.5 \times 9.6$	230 720	8	7731 (hollow)
Large/12nm	$16.5 \times 16.5 \times 9.6$	230 720	12	20 784 (hollow)
Cnt/4 nm	$8.2 \times 8.2 \times 11$	59 040	4	1107

[This article is copyrighted as indicated in the abstract. Reuse of AIP content is subject to the terms at: http://scitation.aip.org/termsconditions. Downloaded to] IP: 131.215.71.79 On: Thu, 17 Oct 2013 14:48:06

separated by a pre-determined distance and a downward velocity (v_{ini}) of the tip. A constant force (F_{res}) in the upward direction is applied to the tip throughout the simulation to mimic the restoring force due to the deflection of the cantilever. In order to avoid the translation of the polymer slab during interaction with the tip, we fix the atomic positions of the atoms located in the bottom 10% of the slab. The mass of the tip is set to 100 ng (by changing the mass of the atoms in the tip), which is a typical value of the cantilever-tip effective mass.[16] The DCS methods model the final dynamics of the tip before interacting with the substrate and the entire process of interaction including indentation and retraction. In the absence of interaction with the substrate, the maximum distance traveled by the tip (D_{max}) in DCS is equal to the ratio

$$D_{max} = \frac{mv_{ini}^2}{2F_{res}}. \quad (1)$$

In all our calculations, we set $D_{max} = 1.85$ nm; that is, our simulations focus on the final 1.85 nm excursion of the tip. The loading rate is controlled in DCS by changing the initial velocity/restoring force pair while keeping D_{max} constant; this loading rate is related to the frequency and amplitude of the cantilever oscillations. Typical dynamic AFM experiments involve frequencies from 5 to 100 KHz with amplitudes ranging from 1 to 100 nm. As a consequence, the last 2 nm of the tip motion range from 10^5 to 10^2 ns. Our simulation, time vary in between 0.1 to 10 ns, one order of magnitude faster than in experiments. As will be shown below, the interaction with the substrate has a small effect on the dynamics of the tip due to the short interaction times and large tip mass.

We define the *nominal* separation distance between the tip and the sample d_{nom} as the distance along the z direction between the lowest atom of the tip and the highest atom of the sample. The *local* distance d_{loc} between the tip and the substrate is defined as that between the lowest atom of the tip and surface right beneath it. The precise determination of the local distance is deduced from the surface topography obtain using a probe as describe in Sec. IV.

C. Quantities of interest

In this study, we focus on two main quantities of interest: the dissipation energy per cycle and the Young's modulus. Both of them are extracted from the tip-sample force-distance curves obtained from the simulations by subtracting the restoring force (F_{ref}, Eq. (1)) to the total force acting on the tip. The dissipation energy is defined as

$$E_{diss} = \int_{cycle} F(z)dz. \quad (2)$$

Young's modulus (E) can be evaluated by fitting the loading part of the force-displacement curves with the Hertz's model[46]

$$F = \frac{4}{3}E\sqrt{Rd^3} \quad (3)$$

with R the radius of the tip and d the penetration depth into the sample. To obtain the Young's modulus, the penetration depth is defined from the point where the force becomes positive after the first attractive interaction during approach (see zone (II) in Figure 4). Our objectives are to characterize how dissipation energy and Young's modulus depend on the conditions of the interaction (e.g., indentation depth and deformation rate) on the local surface topography and their variability.

III. FORCE-DISPLACEMENT CURVES AND LOCAL PROPERTIES

A. Force-displacement curves

The interaction force between the tip and the sample as a function of their separation is one of the main results in non dynamic AFM experiments[47] and can be extracted using models in tapping-mode AFM[7] or T-shaped cantilever as proposed by Sahin and co-workers.[11] Figure 2 shows characteristic force-displacement curves for the three tip diameters studies and, in each system, for various initial separation distances. All cases correspond to an initial tip velocity $v_{ini} = 25\ \mathrm{m.s}^{-1}$, the corresponding restoring force being $F_{res} = 16.89\,N$ (Eq. (1)). The tip-sample separation (along the z direction) is defined so that $d = 0$ nm corresponds to the lowest atom of the tip and the highest atom of the initial surface having the same position. These curves show the viscoelastic nature of the polymer that results in a hysteretic behavior. Reducing the initial separation between tip and sample (causing large penetration depth) leads to similar

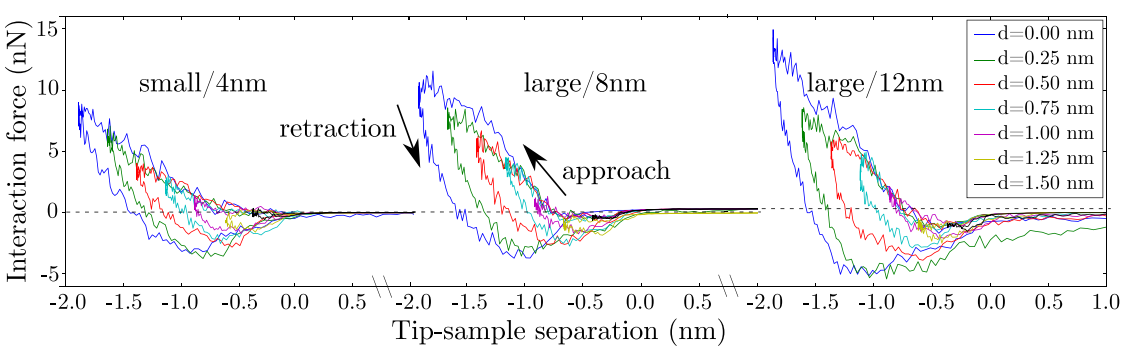

FIG. 2. Interaction force as a function of the tip-sample separation for several nominal initial distances. For the three systems: small/4 nm (left), large/8 nm (middle), and large/12 nm (right). The force and position values used for these curves have been averaged over windows of 10 simulation points for the sake of clarity.

[This article is copyrighted as indicated in the abstract. Reuse of AIP content is subject to the terms at: http://scitation.aip.org/termsconditions. Downloaded to] IP: 131.215.71.79 On: Thu, 17 Oct 2013 14:48:06

approach curves but different retraction behaviors. As expected, larger tip radius of curvature leads to increased attractive and repulsive interaction forces. The curves presented in Figure 2 correspond to indentations at the center of the simulation cell $\{l_x/2, l_y/2\}$. In order to quantify the uncertainties originating from the variability in surface topography and the local molecular structure, we report in supplementary material[44] (Figure S2) the corresponding force-displacement curves located at two different {x,y} locations for the same set of initial separations. We find that the shape of the force-displacement curves and the general trends are the same in all cases.

Figure 3 shows the dissipation energy per contact, obtained by integrating the curves presented on Figure 2 (and Figure S2) using Eq. (2), as a function of the *local* initial distance for the various cases. Dissipation energy increases with increased penetration and, given local distance, the dissipation energy increases with the size of the tip. The magnitude of the dissipation energy compute in this work is in good agreement with experiments.[48] The analysis of the local Young's modulus will be presented below and will include a larger range of data points.

B. Effect of the loading rate

In this section, we focus on the effect of loading rate on the tip-sample interaction and the effective properties obtained; given the long simulation times involved we focus on the small/4 nm system. Figure 4 shows the time evolution of the interaction force and the velocity from one of our simulations; we divide each interaction cycle in four periods: (I) weak attractive interaction while the tip moves downward; the attractive van der Waals interaction accelerates the tip towards the substrate and increases the energy of the tip; (II) the interaction force is repulsive while the tip moves downward; in this case, the polymer helps stop the tip, energy is transferred from the tip to the substrate; (III) the interaction force is repulsive while the tip moves upward; the polymer pushes the tip up and transfers energy back to the tip; (IV) the interaction force is attractive (adhesive) while the tip moves upward; the polymer holds the tip back during the last stage of retraction as van der Waals bonds are broken and

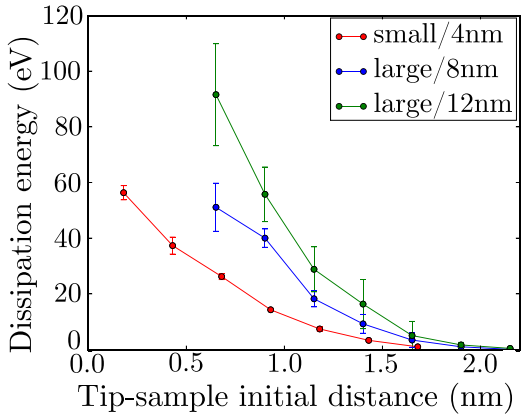

FIG. 3. Dissipation energy as a function of the local distance for different diameter of the tip. The error bar is computed from the indentation at three different locations (data from Figures 2 and S2).

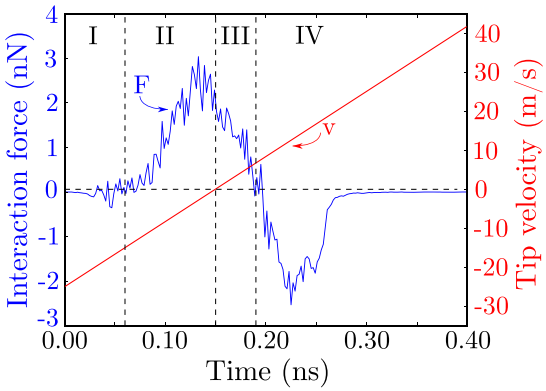

FIG. 4. Tip-polymer interaction force (blue, left axis), velocity of the tip (red, right axis) as a function of the simulation time (small/4 nm system). The initial tip-sample separation d = 0.75 nm.

energy is transferred from the tip to the substrate. Due to the large effective mass of the tip, the tip-sample interaction does not change the dynamics of the tip noticeably as is apparent in the velocity shown in Figure 4.

We characterize the role of loading rate by studying a variety of initial velocities (and corresponding restoring force) by keeping the ratio $mv_{ini}^2/2F_{res}$ constant (the maximum travel of the tip D_{max}, Eq. (1)). Figure 5 shows the interaction force as a function of the simulation time for different initial velocity/force pairs $\{v_{ini}, F_{res}\}$. All these simulations start at the same nominal separation d = 0.25 nm. Our results show that slower loading rates result in smaller repulsive interaction during approach and larger attractive interaction during approach and retraction. To understand the molecular origin of the increased adhesion with decreasing loading rate we show, in Figure 6, molecular structures of the tip and sample corresponding to the slowest (top panels) and fastest (bottom panels) loading rates. Left panels show the configurations corresponding to zero tip velocity (maximum indentation) and the right ones correspond to maximum attractive force during retraction. We observe that the effective contact area between the tip and the sample is larger for the slow loading rate; the slower motion of the tip provides additional time for the polymer to relax around it and

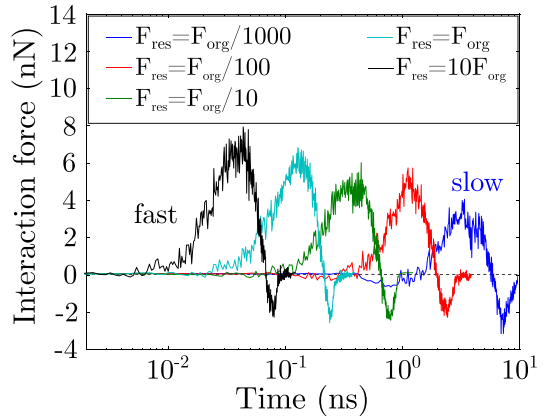

FIG. 5. Tip-polymer interaction force as a function of the logarithmic time for different loading rates. The force values used for these curves have been averaged over windows of 10 simulation points for the sake of clarity. The subscript *org* stands for the *original* rate introduced in Sec. III.

[This article is copyrighted as indicated in the abstract. Reuse of AIP content is subject to the terms at: http://scitation.aip.org/termsconditions. Downloaded to] IP: 131.215.71.79 On: Thu, 17 Oct 2013 14:48:06

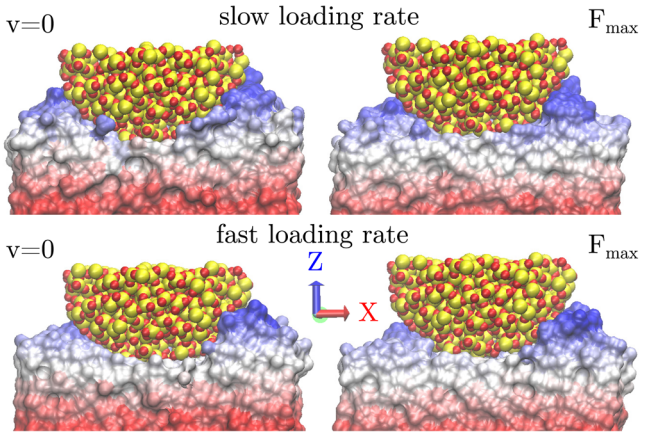

FIG. 6. Snapshot of the tip-polymer structure at zero tip velocity (left) and maximum attractive force (right) for the two loading rates: $F_{res} = F_{org}/100$ (top) and $F_{res} = 10F_{org}$ (bottom) in the {xz} plane. The color scale represent the height (z) and ranges from 0.0 nm (red) to 2.5 nm (blue).

increase the contact area. As a consequence, the repulsion force is smaller and adhesion is larger for the slower loading rates. At higher strain rates, elastic behavior dominates; while at lower strain rates, the viscous effects play a more dominant role.

In the DCS methodology, the initial velocity and the restoring force determine the maximum distance traveled by the tip in the absence of interactions with the substrate. As discussed above, even for the slower rate studied, the trajectory of the tip is not affected significantly by the interactions with the slab. However, slower loading rates lead to longer interaction timescales during which the polymer undergoes relaxation underneath the tip; notice the attractive interactions during approach in Figure 5 present in the slowest simulation and absent in the others. As a consequence, we find that slower loading rates lead to smaller indentation depths defined as the distance between the beginning of repulsive interaction and the maximum tip displacement; from faster to slower loading rates, we find indentation depths of d = 1.35, 1.31, 1.29, 0.91, and 0.78 nm, respectively. At the same time, slower interactions lead to polymer relaxation during compression and a reduction in maximum repulsive force: $F_{max} = 11.4$, 10.9, 9.5, 9.0, and 7.5 nN from faster to slower loading rates. The combination of smaller indentation and forces with decreasing loading lead to the following effective Young's moduli (from faster to slower rates): E = 2.8, 2.4, 2.2, 3.8, and 3.2 GPa, respectively. Numerical uncertainties in the Young's modulus values can be evaluated by slightly reducing the number of data points used to fit the Hertz law; this analysis leads to uncertainties of the order of 0.1 GPa. Interestingly, we find that slower loading rates lead to higher effective stiffness. This interesting result is, perhaps, counter-intuitive and reflects the inability of the Hertz model to capture adhesion and non-elastic processes as well as molecular-level details that dominate small indentations and the challenges in the interpretation of AFM results. These results highlight the extreme care that should be exercised in analyzing dynamical AFM data especially for small indentations.

IV. SURFACE TOPOGRAPHY AND PROPERTY MAPS

One of the most impressive and technologically important capabilities of dynamical AFM is to produce local properties maps[49] with nanoscale resolution (tens of nm (Ref. 13)). However, the link between the observables and the actual property is still not fully understood. In this section, we determine the surface topography and use it to compute surface property maps both for elasticity and energy dissipation.

A. Surface topography maps

In order to correlate the effective substrate properties obtained from the force-displacement curves with the local surface topography, we compute a surface height map by scanning the polymer surface with the tip. With this information, we will compute precise local distances from the tip to the surface and local surface curvature. Here, we assume that the timescales associated with changes in surface topography are long compared with our simulations; an assumption that seems to be valid based on our observations. To compute the topography map, we set both the polymer and the tip as rigid bodies. In order to describe the roughness with precision, we divide the cross-sectional area with a regular 100×100 grid. At each grid point, we determine the surface height as the tip location where the interaction between the two rigid bodies results in a repulsive force of 0.4 nN. This is an arbitrary value but due to the stiffness of repulsive interactions, the resulting topography is only weakly dependent on this choice. We show in the supplementary material[44] (Figure S4) that changing this threshold does not affect the description of the topography. Since the only goal of this exercise is to determine the location of surface, we use a simple Lennard-Jones potential[50] to describe the interaction between atoms in the polymer and tip with a cutoff of 0.25 nm (since we are only interested in the repulsive part of the interaction). Two surfaces ($H(x, y)$) are shown in Figure 7(a) corresponding to the small/4 nm and the cnt/4 nm systems.

Despite the large diameter of the tip compared to the dimension of the samples (~2/3 of the edge length for the small/4 nm system), the topography maps exhibit high resolution. We show in supplementary material[44] (Figure S3) that the topography maps are rather insensitive to the tip size. Several key features of the polymer samples are revealed by these topography maps. The small/4 nm sample shows a surface roughness of approximately 1 nm while the presence of the CNT in cnt/4 nm creates a hump on the surface (~1.6 nm of roughness for this sample).

B. Surface properties

With the surface topography characterized, we now compute maps of dissipation energy and Young's modulus using molecular dynamic simulation as described in Sec. II. We introduce two mapping modes: (i) in the *constant height mode* (CHM), the {x,y} cross-sectional area is divided in a square 10×10 grid; and at each point of this grid, an indentation simulation is performed starting at the same absolute height z_0 (corresponding to the initial nominal separation

[This article is copyrighted as indicated in the abstract. Reuse of AIP content is subject to the terms at: http://scitation.aip.org/termsconditions. Downloaded to] IP: 131.215.71.79 On: Thu, 17 Oct 2013 14:48:06

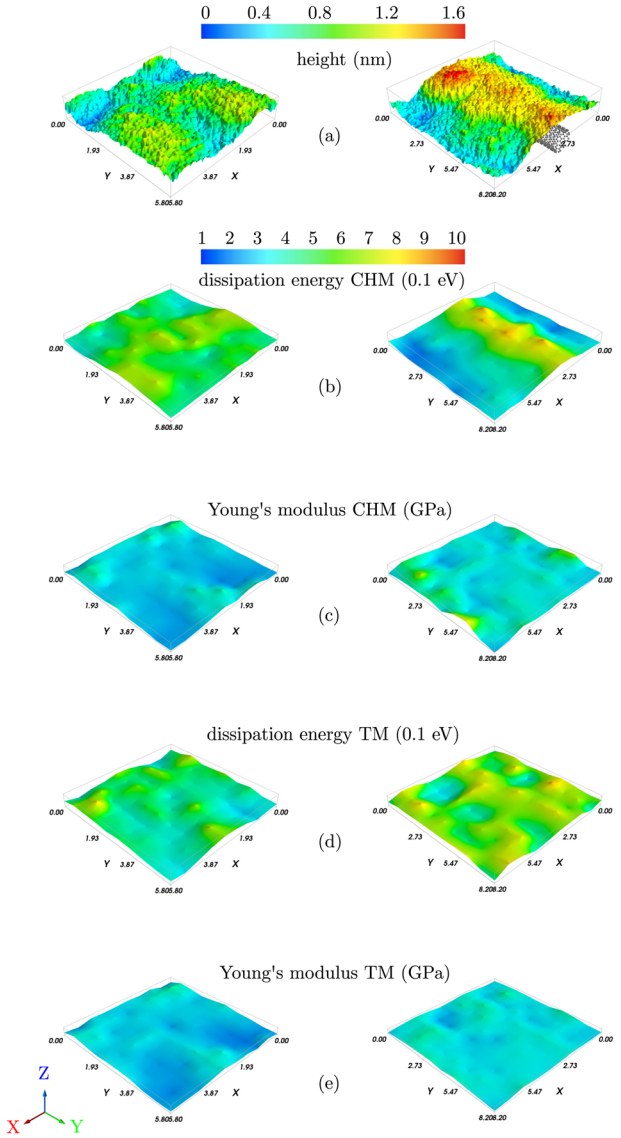

FIG. 7. Properties maps of the two samples (small/4 nm: left, cnt/4 nm: right): (a) Topography map; (b) Dissipation map in CHM; (c) Young's modulus map in CHM; (d) Dissipation map in TM; (e) Young's modulus map in TM. A unique color bar is related to the properties and refers to 0.1 eV in the case of dissipation energy and GPa for Young's modulus.

$d_{nom} = 0.0$ nm); (ii) in the *topographic mode* (TM), the simulations are performed starting at different z_i positions following the surface topography, keeping the local separation distance at time zero to $d_{loc} = 0.5$ nm. While this second approach does not correspond to any dynamic AFM operation mode, it can be thought of as an approximation to constant force operation. The tip tracks the local topography, so each indentation achieves approximately the same depth and repulsive force. Due to the computational intensity of these runs (100 simulations per map), we only investigate the small/4 nm and the cnt/4 nm systems. The property maps are shown on Figures 7(b)–7(e).

Averaging over all measurements in the small/4 nm sample, we obtain a dissipation energy of $\bar{E}_{diss} = 47.7 \pm 7.6$ eV and a Young's modulus $\bar{E} = 2.1 \pm 0.6$ GPa in CHM. In case of TM, the mean dissipation energy is $\bar{E}_{diss} = 41.8 \pm 8.2$ eV and the mean Young's modulus $\bar{E} = 2.0 \pm 0.5$ GPa. Both mapping modes result in similar means values and standard deviations. While the variation in indentation distance in CHM can contribute to the observed variability in local properties, in the case of TM, the variability is a consequence of the local variation in the molecular structure and surface topography. Interestingly, the presence of asperities correlates with local minima in Young's modulus maps for both mapping modes. This can be explained by the convexity of the surface, which leads to apparent softening; the Hertz solution used to extract Young's moduli applies to a perfectly flat surface.

The local property maps show that the sub-surface CNT affects the measured quantities. We observe larger dissipation energies when the indentation proceeds over the CNT (cnt/4 nm system). This last statement is true in both mapping modes (CHM and TM); indentations over the CNT lead to dissipation up to 90 eV; these values are higher than those computed far from the CNT or in the small/4 nm sample. Several factors contribute to the force-displacement curve shape and consequently to energy dissipation: the stiffness of the substrate (maximum interaction force), the adhesion between the tip and the sample (attractive force), and the relaxation processes that occur in the substrate (the width of the force displacement curve). Even though the CNT itself is perfectly elastic, its presence leads to more dissipation; we attribute this to the higher local stiffness that increases the force and relaxation processes between the CNT and polymer; a molecular analysis of these processes is beyond the scope of this paper.

Figures 8 and 9 compile all calculations of dissipation energy and Young's modulus as a function of indentation depth (data from CHM simulations). We classify the indentations as: over the CNT (red), in the cnt/4 nm sample but away from the CNT (green) and from the small/4 nm case (blue). The slight difference in the range of indentation depths for the two systems is a consequence of the difference in surface roughness between the two cases (1 nm for the small/4 nm versus 1.6 nm for the cnt/4 nm). As noticed before (see Figure 3), the overall dissipation energy increases as the local distance decreases (increasing the indentation

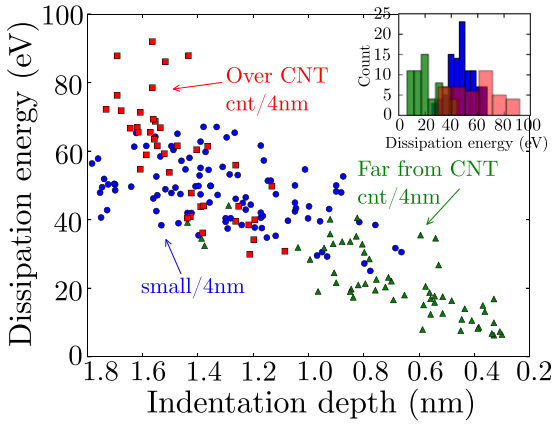

FIG. 8. Dissipation energy as a function of the indentation depth (blue circles: neat PMMA, green triangle: far from the CNT, red squares: over the CNT). Distributions of the dissipation energies per region of indentation (right top panel).

[This article is copyrighted as indicated in the abstract. Reuse of AIP content is subject to the terms at: http://scitation.aip.org/termsconditions. Downloaded to] IP: 131.215.71.79 On: Thu, 17 Oct 2013 14:48:06

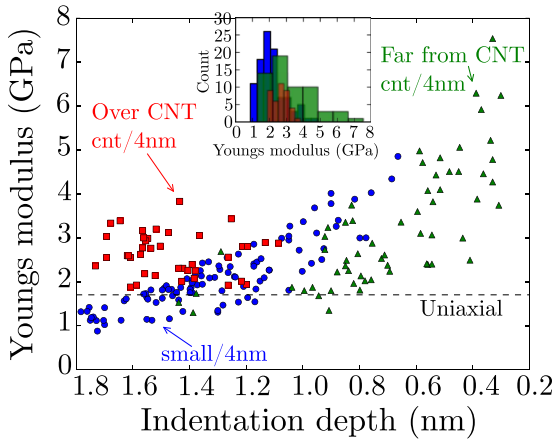

FIG. 9. Young's modulus as a function of the indentation depth (blue circles: neat PMMA, green triangle: far from the CNT, red squares: over the CNT). Distributions of the Young's moduli per region of indentation (middle top panel). The dashed line represents the Young's modulus extracted from uniaxial tension test (1.7 GPa).

depth). Moreover, we find larger dissipation energy when the indentations proceed over the CNT ($\bar{E}_{diss} = 58.6 \pm 16.4$ eV) than far from it ($\bar{E}_{diss} = 21.7 \pm 10.1$ eV).

Figure 9 shows that the effective Young's modulus extracted from indentations increase with decreasing indentation depth. The dashed line represents the Young's modulus calculated from an uniaxial deformation of the entire simulation cell (1.7 GPa). Our results indicate that a minimum indentation depth of approximately 1.2 nm is needed to extract meaningful values of Young's modulus; we attribute this observation to the fact that the expression used to extract E is derived from continuum mechanics and the physics of very small indentations is dominated by atomic processes. This effect has been observed in metal-metal interactions.[21] Indentations over the CNT lead to higher Young's moduli values especially for large indentations where the CNT is affected more pronouncedly.

Our results show that a combination of both increased dissipation and stiffness in surface property maps can be used as an indicator of the presence of a stiff sub-surface reinforcement in the sample.

V. CONCLUSIONS

In summary, we used MD simulations to characterize the interaction of a silica tip and an amorphous PMMA substrate under conditions relevant for dynamic AFM. The DCS methodology and realistic size of the system provide conditions close to experimental setups. Interestingly, the timescales achievable today with MD simulations are close to those in experiments.

The shape and amplitude of the force-displacement curves as well as the corresponding values of the dissipation energies consequence of the viscoelastic behavior of the amorphous polymer predicted by our simulations are in good agreement with continuum model of dynamic AFM[15,48] and experiments.[11]

In our analysis, we characterize how surface topography and sub-surface phases affect the local properties of the surface extracted from the force-displacement curves. Correlating surface topography and local property is now possible experimentally opening exciting applications.[13] The results presented in this paper show that the physical properties extracted from dynamic AFM (dissipation energy and Young's modulus) are not only dependent on the substrate and rate of deformation but are also strongly dependent on the amount of indentation, local surface topography, and also reflect local property variations of the substrate (see differences between the maps in CHM and TM in Figure 7). Finally, the property map analysis of the composite system shows relevant differences in the properties close and far to the CNT, which allow the spatial localization of sub-surface reinforcements.

ACKNOWLEDGMENTS

This work was supported by the Dow Chemical Company and the US NNSA Center for the Prediction of Reliability, Integrity and Reliabilty of Microsystems (PRISM). Computational resources of nanoHUB.org and useful discussions with A. Raman are gratefully acknowledged.

[1]G. Binnig, C. F. Quate, and C. Gerber, Phys. Rev. Lett. **56**, 930 (1986).
[2]G. Binnig, H. Rohrer, C. Gerber, and E. Weibel, Phys. Rev. Lett. **49**, 57 (1982).
[3]F. J. Giessibl, Rev. Mod. Phys. **75**, 949 (2003).
[4]Y. Martin, C. C. Williams, and H. K. Wickramasinghe, J. Appl. Phys. **61**, 4723 (1987).
[5]Q. Zhong, D. Inniss, K. Kjoller, and V. Elings, Surf. Sci. **290**, L688 (1993).
[6]C. Moller, M. Allen, V. Elings, A. Engel, and D. J. Moller, Biophys. J. **77**, 1150 (1999).
[7]R. Garcia and R. Perez, Surf. Sci. Rep. **47**, 197 (2002).
[8]S. Basak and A. Raman, Appl. Phys. Lett. **91**, 064107 (2007).
[9]S. N. Magonov and D. H. Reneker, Ann. Rev. Mater. Sci. **27**, 175 (1997).
[10]F. Moreno-Herrero, J. Colchero, J. Gómez-Herrero, and A. M. Baró, Phys. Rev. E **69**, 031915 (2004).
[11]O. Sahin, S. Magonov, C. Su, C. F. Quate, and O. Solgaard, Nat. Nanotechnol. **2**, 507 (2007).
[12]O. Sahin and N. Erina, Nanotechnology **19**, 445717 (2008).
[13]S. Husale, H. H. J. Persson, and O. Sahin, Nature **462**, 1075 (2009).
[14]A. Raman, J. Melcher, and R. Tung, Nano Today **3**, 20 (2008).
[15]J. Melcher, S. Hu, and A. Raman, Rev. Sci. Instrum. **79**, 061301 (2008).
[16]S. D. Solares and H. Hlscher, Nanotechnology **21**, 075702 (2010).
[17]D. Kiracofe, J. Melcher, A. Raman, S. Balasubramaniam, S. D. Johnson, and S. Hu, "Veda: Virtual environment for dynamic afm" (2012), https://nanohub.org/resources/veda.
[18]N. F. Martinez, W. Kaminski, C. J. Gomez, C. Albonetti, F. Biscarini, R. Perez, and R. Garcia, Nanotechnology **20**, 434021 (2009).
[19]R. Bechstein, C. Gonzalez, J. Schutte, P. Jelinek, R. Perez, and A. Kuhnle, Nanotechnology **20**, 505703 (2009).
[20]A. Campbellova, M. Ondracek, P. Pou, R. Perez, P. Klapetek, and P. Jelinek, Nanotechnology **22**, 295710 (2011).
[21]H. Kim, G. Venturini, and A. Strachan, J. Appl. Phys. **112**, 094325 (2012).
[22]H. N. Pishkenari and A. Meghdari, Curr. Appl. Phys. **10**, 583 (2010).
[23]U. Landman, J. Vacuum Sci. Technol. B **9**, 414 (1991).
[24]G. Patzold, T. Hapke, A. Linke, and D. W. Heermann, Thin Solid Films **295**, 199 (1997).
[25]M. Katagiri, D. Patrick, and R. Lynden-Bell, Surf. Sci. **431**, 260 (1999).
[26]B. Bat-Uul, S. Fujii, T. Shiokawa, T. Ohzono, and M. Fujihira, Nanotechnology **15**, 710 (2004).
[27]K. Yashiro, A. Furuta, and Y. Tomita, Comput. Mater. Sci. **38**, 136 (2006).
[28]J. Shimizu, L. Zhou, and H. Eda, *in Proceedings of the 35th International MATADOR Conference*, edited by S. Hinduja and K.-C. Fan (Springer, London, 2007), pp. 271–274.
[29]W.-J. Lee, S.-P. Ju, and C.-H. Cheng, Langmuir **24**, 13440 (2008).

[This article is copyrighted as indicated in the abstract. Reuse of AIP content is subject to the terms at: http://scitation.aip.org/termsconditions. Downloaded to] IP: 131.215.71.79 On: Thu, 17 Oct 2013 14:48:06

[30]W. Wang, K. A. Kistler, K. Sadeghipour, and G. Baran, Phys. Lett. A **372**, 7007 (2008).
[31]M. Chandross, C. D. Lorenz, M. J. Stevens, and G. S. Grest, Langmuir **24**, 1240 (2008).
[32]M. Solar, H. Meyer, C. Gauthier, O. Benzerara, H. Pelletier, R. Schirrer, and J. Baschnagel, J. Phys. D: Appl. Phys. **43**, 455406 (2010).
[33]T. Trevethan and L. Kantorovich, Nanotechnology **16**, S79 (2005).
[34]R. Alizadegan, A. Liao, F. Xiong, E. Pop, and K. Hsia, Nano Res. **5**, 235 (2012).
[35]H. N. Pishkenari, S. H. Mahboobi, and A. Meghdari, J. Phys. D: Appl. Phys. **44**, 075303 (2011).
[36]N. L. Anderson, R. P. Vedula, P. A. Schultz, R. M. Van Ginhoven, and A. Strachan, Phys. Rev. Lett. **106**, 206402 (2011).
[37]P. Steve, J. Comput. Phys. **117**, 1 (1995).
[38]S. L. Mayo, B. D. Olafson, and W. A. Goddard, J. Phys. Chem. **94**, 8897 (1990).
[39]R. W. Hockney and J. W. Eastwood, *Computer Simulation Using Particles* (Taylor & Francis, 1989).
[40]M. Tuckerman, B. J. Berne, and G. J. Martyna, J. Chem. Phys. **97**, 1990 (1992).
[41]C. Li and A. Strachan, Polymer **52**, 2920 (2011).
[42]C. Li and A. Strachan, Macromolecules **44**, 9448 (2011).
[43]E. Jaramillo, N. Wilson, S. Christensen, J. Gosse, and A. Strachan, Phys. Rev. B **85**, 024114 (2012).
[44]See supplementary material at http://dx.doi.org/10.1063/1.4820256 for details.
[45]K. Yae-ji, L. Keng-Hua, and A. Strachan, Modell. Simul. Mater. Sci. Eng. **21**, 065010 (2013).
[46]K. L. Johnson and K. L. Johnson, *Contact Mechanics* (Cambridge University Press, 1987).
[47]B. Cappella and G. Dietler, Surf. Sci. Rep. **34**, 1 (1999).
[48]R. Garcia, C. J. Gomez, N. F. Martinez, S. Patil, C. Dietz, and R. Magerle, Phys. Rev. Lett. **97**, 016103 (2006).
[49]H. Assender, V. Bliznyuk, and K. Porfyrakis, Science **297**, 973 (2002).
[50]J. E. Jones, Proc. R. Soc. London, Ser. A **106**, 463 (1924).

[This article is copyrighted as indicated in the abstract. Reuse of AIP content is subject to the terms at: http://scitation.aip.org/termsconditions. Downloaded to] IP: 131.215.71.79 On: Thu, 17 Oct 2013 14:48:06